sustainability

MDPI

Article

Evaluation of the Melting Performance in a Conical Latent Heat Thermal Unit Having Variable Length Fins

Mohammad Ghalambaz [1,2], S.A.M. Mehryan [3], Mahboobeh Mahdavi [4], Obai Younis [5,6] and Mohammad A. Alim [7,*]

1 Metamaterials for Mechanical, Biomechanical and Multiphysical Applications Research Group, Ton Duc Thang University, Ho Chi Minh City 758307, Vietnam; mohammad.ghalambaz@tdtu.edu.vn
2 Faculty of Applied Sciences, Ton Duc Thang University, Ho Chi Minh City 758307, Vietnam
3 Young Researchers and Elite Club, Yasooj Branch, Islamic Azad University, Yasooj 7591493686, Iran; alal171366244@gmail.com
4 Mechanical Engineering Department, Gannon University, 109 University Square, Erie, PA 16541, USA; mahdavi001@gannon.edu
5 Department of Mechanical Engineering, College of Engineering at Wadi Addwaser, Prince Sattam Bin Abdulaziz University, Wadi Addwaser 11991, Saudi Arabia; oubeytaha@hotmail.com
6 Department of Mechanical Engineering, Faculty of Engineering, University of Khartoum, Khartoum 11111, Sudan
7 School of Engineering, Design and Built Environment, Western Sydney University, Kingswood, NSW 2747, Australia
* Correspondence: M.Alim@westernsydney.edu.au

Abstract: A conical shell-tube design with non-uniform fins was addressed for phase change latent heat thermal energy storage (LHTES). The shell was filled with nano-enhanced phase change material (NePCM). The cone aspect ratio of the shell and the fins aspect ratio were adopted as the geometrical design parameters. The type and volume fraction of the nanoparticles were other design parameters. The investigated nanoparticles were alumina, graphite oxide, silver, and copper. The finite element method was employed to solve the natural convection flow and phase change thermal energy equations in the LHTES unit. The Taguchi optimization method was utilized to maximize the melting rate in the unit. Two cases of ascending and descending conical shells were investigated. The outcomes showed that the shell-aspect ratio and fin aspect ratio were the most important design parameters, followed by the type and concentration of nanoparticles. Both ascending and descending designs could lead to the same melting rate at their optimum design. The optimum design of LHTES could improve the melting rate by up to 18.5%. The optimum design for ascending (descending) design was a plain tube (a cone aspect ratio of 1.17) filled by 4.5% alumina-Bio-PCM (1.5% copper-Bio-PCM).

Keywords: latent heat thermal energy storage (LHTES); conical shape; non-uniform fin; nano-enhanced phase change material (NePCM)

Citation: Ghalambaz, M.; Mehryan, S.A.M.; Mahdavi, M.; Younis, O.; Alim, M.A. Evaluation of the Melting Performance in a Conical Latent Heat Thermal Unit Having Variable Length Fins. *Sustainability* **2021**, *13*, 2667. https://doi.org/10.3390/su13052667

Academic Editor: Grigorios L. Kyriakopoulos

Received: 29 January 2021
Accepted: 23 February 2021
Published: 2 March 2021

1. Introduction

Offering a high energy density and nearly isothermal operation, a latent heat thermal energy storage (LHTES) system is often a preferable choice over other thermal energy storage systems. LHTES systems use a phase change material (PCM) as the storage medium. Thermal energy is stored when the solid PCM undergoes a phase change to liquid, and then when the phase change process is reversed, i.e., the molten PCM solidifies, the stored energy is released. The performance of an LHTES system might be degraded due to the low thermal conductivity of the PCMs; therefore, implementation of heat transfer enhancement techniques may become necessary. The heat transfer enhancement techniques can be divided into two categories: (1) improving the thermal physical properties of the

PCM by dispersion of highly conductive micro- and nano-sized particles and (2) using highly conductive inserts such as metal fins, heat pipes, and porous structures [1–3].

In recent years, the dispersion of highly conductive nanoparticles into the PCM has been utilized to improve the unit performance during the charging and discharging processes [4]. Various nanoparticles such as pure metals [5,6], metal oxides [7,8], and carbon-based nanoparticles [9] have been considered. The results of these studies have denoted that the volume fraction of nanoparticles plays an important role in controlling the melting and solidification processes. The impact of graphene nanoparticles on the melting process of various PCMs in a square cavity was studied by Kant et al. [10]. It was found that using nanoparticles improves the conductive heat transfer while weakening the natural convection heat transfer. The overall results, however, indicated that there is a reduction in the melting time.

Lin and Al-Kayiem [11] have experimentally evaluated the effects of incorporating Cu nanoparticles on the thermal characteristics of a paraffin wax during the melting and solidification processes. They have reported that the dispersion of copper nanoparticles with a concentration of 2.0% by weight leads to a 46.3% increase in the thermal conductivity of the composite PCM.

A numerical study performed by Mahdi and Nsofor [12] indicated that the discharging time is reduced by 8–20% of alumina nanoparticles with volume concentrations of 8–13%, respectively, are used. The melting of paraffin in the presence of copper nanoparticles in an elliptical capsule was numerically studied by Boukani et al. [13]. Three volumetric nanoparticle concentrations of 0%, 1%, and 3% and three container aspect ratios of 2, 1, and 0.5 were employed. The results revealed that, at a fixed aspect ratio, the presence of nanoparticles improves the performance of the system.

As mentioned earlier, fins improve the distribution of heat through high thermal conductive extended surfaces, and thus, they reduce a thermal resistance in an LHTES. Gharebaghi and Sezai [14] studied the influence of aluminum fin arrays on the melting process of paraffin wax in a rectangular container. The results showed that the melting time and the stored energy were impacted by the spacing and the height of the fin arrays. The performance of a fin and tube LHTES system was experimentally investigated by Rahimi et al. [15]. The heat transfer fluid (HTF) flowed inside a spiral tube, and plate fins were used to increase the heat transfer rate. The results showed that the presence of fins notably reduces the melting time, and the closer the fins, the shorter the melting time. Yang et al. [16] simulated the phase change heat transfer in an annularly finned LHTES. The authors discussed the fin quantity, height, and thickness for optimal charging of a shell-tube LHTES unit. The authors considered the contribution of natural convection on the overall melting. It was found that the presence of fins diminishes the charging time by 65%.

In addition to plate and circular fins, the use of longitudinal fins has also been studied by researchers [17,18]. In a research study conducted by Kazemi et al. [19], the effect of the longitudinal fin angle was evaluated. The results showed that a lower melting time was obtained when the angle was increased from 60° to 120° for the case with three fins. However, when two fins were used, increasing the angle from 45° to 150° deteriorated the performance of the system. The effect of fin angle was also investigated by Deng et. al. [20]. In an experimental study carried out by Rathod and Banerjee [21], the augmentation in heat transfer was studied in a shell and tube heat exchanger. Three longitudinal fins were installed at the outer surface of the inner tube to increase the heat transfer surface. The results showed that the decreased percentage in melting time relies on the heat transfer fluid (HTF) inlet temperature.

The available studies in the literature have reported that combining heat transfer enhancement techniques can lead to a better heat transfer performance of the storage unit [22,23]. Studies can be found using a combination of fins and heat pipes [24], nanoparticles and fins [25,26], nanoparticles and metal foams [27], metal foams, and heat pipes [28]. Ren et al. [29] studied the application of triangular fins in a rectangular LHTES with and

without the presence of nanoparticles in the PCM. It was reported that using triangular fins was more efficient than solely using nanoparticles. In addition, the arrangement with long and narrow fins that were appropriately spaced provided a higher energy storage efficiency. Li et al. [30] studied the melting of graphene nanoplatelets in 1-tetradecanol in a rectangular enclosure. They investigated the impact of various mass fraction of nanoparticles and enclosure aspect ratio on the melting behavior of nano-enhanced phase change material (NePCM). They found that a slender enclosure could be better for application of NePCMs.

Darzi et al. [31] studied the influence of copper nanoparticles in three horizontal double pipes LHTES systems. The three configurations included a circular shell with an elliptical inner pipe, a cylindrical inner pipe, and a finned cylindrical inner pipe. The effect of the number of fins, as well as the orientation of the ellipse, were evaluated for different concentrations of nanoparticles. Mahdi and Nsofor [22] studied the combined effects of nanoparticles and longitudinal fins in a shell and tube LHTES unit. Fins were added both on the outer surface of the inner pipe and the inner wall of the shell. It was found that better solidification time was achieved for the case with only fins when compared to the cases with only nanoparticles or with a combination of both.

The literature review of the available studies shows that natural convection heat transfer plays a role in the system's performance, especially during the melting process. It should be noted that the significance of these effects is influenced by various parameters such as PCM type, container configuration, and container orientation. Shell and tube latent heat thermal energy storage systems are one of the common types of LHTES systems and are considered for the current study. The heat transfer fluid flows inside the inner tube, while the PCM is located in the shell. As the container is located vertically, the melting process will be governed by natural convection heat transfer. Therefore, due to the upward motion of the molten PCM, more melting will occur at the top of the container as compared to the lower section. To provide a more uniform and accelerated melting process, a conical shell is considered. To further accelerate the melting process, combinations of fins and dispersed nanoparticles are used as the heat transfer enhancement technique.

As mentioned earlier, fins contribute to the enhanced heat transfer process by providing more surface area. The level of improvement varies based on the design of the shell and the fins geometry. In some cases, the presence of the fins may dampen the natural convection flows, which may suppress some of the potential improvements. On the other hand, using dispersed nanoparticles increases the effective thermal conductivity of the NePCM, but it also increases the viscosity of NePCM, which consequently limits the liquid motion and natural convection. By considering these factors, finding an ideal configuration of an LHTES system and enhancement techniques is a crucial task. Thus, the present study aims to address the melting heat transfer in a conical shape LHTES and its optimum design for the shell's aspect ratio, fins' aspect ratio, type of nanoparticles, and volume fractions of nanoparticles for the first time.

2. Mathematical Model

A conical latent heat thermal energy storage (LHTES) system, filled with a nano-enhanced phase change material (NePCM), is illustrated in Figure 1. The general shape of the LHTES' shell is a conical shape that could be a descending or ascending conical enclosure. The fins can also be uniform, ascending, or descending. Based on the shape of the LHTES unit shell here, two types of the general design were adopted. A view of the ascending conical and the descending conical LHTES units are depicted in Figure 1a,c, respectively. The cylindrical design is a special case of each of these two designs and is illustrated in Figure 1b. Assuming the LHTES volume is constant, the radius of the cross-section of the system along the z-direction can be descending, constant, or increasing. Furthermore, the height of the connected copper fins can be changed according to the shape of the system. The height of the LHTES is L = 200 mm, and the radius of the normal system with a uniform circular cross-section (depicted in Figure 1b) is R_o = 50 mm. In the conical LHSS, the lower radius of the cross-section, i.e., R_{dc}, is defined base on the aspect ratio,

i.e., $AR_c = R_{dc}/\ R_o$. Also, the length of the lowest fin, i.e., w_{df}, is $AR_f \times w_{uf}$ in which w_{uf} is the length of identical fins. It is worth noting that the volume of all fins is considered a constraint. Figure 2 shows the structural specification of the unit. Water, as the heat transfer fluid has a high temperature, enters the tube and the energy is transferred to the composite NePCM through the tube wall. The NePCM contains the highly thermal conductive nano-additives added to the coconut oil as the base PCM. The thermophysical properties of the base PCM, HTF, and the fins are listed in Table 1. As tabulated in Table 2, the nano additives dispersed in the PCM can separately be Al_2O_3, GO, Ag, and Cu. Furthermore, the axisymmetric structure of the system allows the problem to be solved in 2D space.

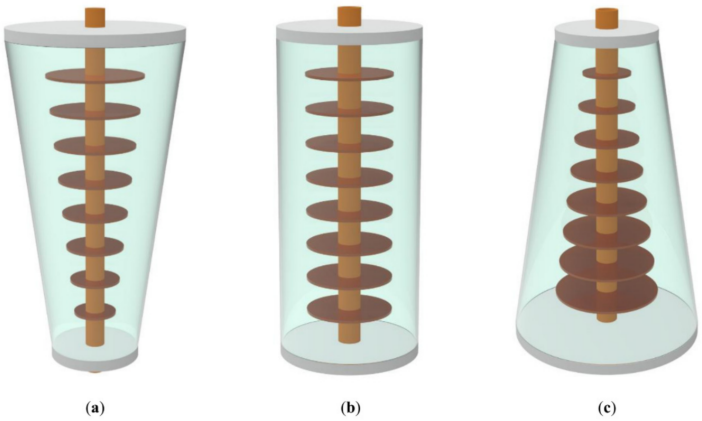

Figure 1. Latent heat thermal energy storage (LHTES) unit: (**a**) ascending conical; (**b**) cylinder; (**c**) descending conical.

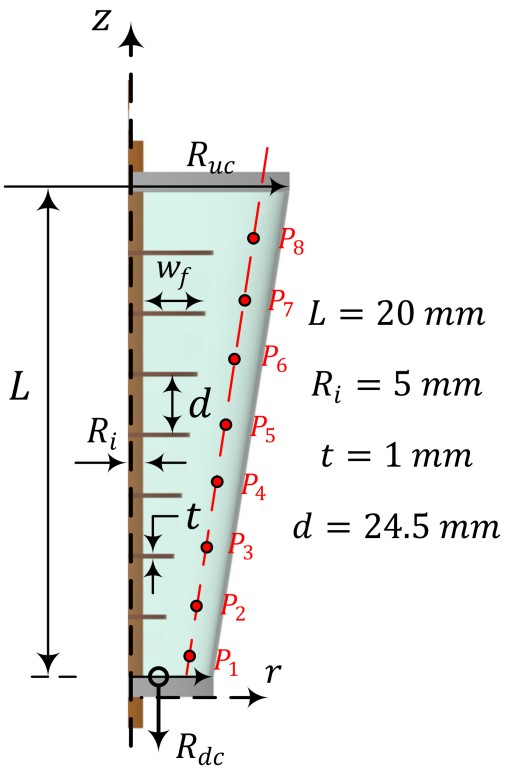

Figure 2. Structural specifications of the LHTES; coordinate of P_i is $(R_{dc} + a(i-2/3)h_{sf} - 2R_i, (i-2/3)h_{sf})$.

Table 1. Thermophysical properties of the coconut oil and the nano-additives [32,33].

Properties	Bio-Based PCM		Water as HTF	Solid Fin
	Liquid	Solid		
C_p (JkgK^{-1})	2010	3750	4178	386
η (Nsm^{-2})	326×10^{-4}	Non-defined	705×10^{-6}	Non-defined
ρ (kgm^{-1})	914	920	993.73	8900
k (Wm^{-1}K^{-1})	166×10^{-3}	228×10^{-3}	623×10^{-3}	401
$T_{melting}$ (K)	Non-defined	297	Non-defined	Non-defined
L_{PPCM} (Jkg^{-1})	103e3	Non-defined	Non-defined	Non-defined

Table 2. Nanoparticles dispersed in the phase change material [34–36].

Properties	GO	Al_2O_3	Cu	Ag
ρ (kgm^{-1})	1800	3600	8960	10,500
C_p (JkgK^{-1})	717	765	385	235
k (Wm^{-1}K^{-1})	5000	36	400	429
β (K^{-1})	28.4×10^{-5}	7.8×10^{-6}	16.7×10^{-6}	18.9×10^{-6}

For the NePCM domain, the enthalpy-porosity technique is used to model the melting flow. The controlling equations, i.e., the equations describing mass, momentum, and energy conservations, are:

$$\frac{D\rho}{Dt} = 0; \tag{1}$$

$$\rho_{LNePCM}\frac{D\vec{V}}{Dt} = -\nabla p + \eta_{LNePCM}\nabla^2\vec{V} + A_m\frac{(1-s(T))^2}{10^{-3}+s(T)^3}\vec{V} + \vec{g}\rho_{LNePCM}\beta_{LNePCM}\left(T - T_{melting}\right), \tag{2}$$

where the velocity vector ($\vec{V}$) and the pressure field (p) are the dependent variables. The density (ρ), volume expansion coefficient (β), and dynamic viscosity (μ) are the thermophysical properties. The gravity direction ($\vec{g}$) is toward the bottom, and its component in the horizontal direction is zero. The subscripts *LNePCM* shows the liquid NePCM and A_m (O(10^6)) is a large number to procurance the value of the source term. The liquid fraction (s) is a temperature dependent-function:

$$s(T) = \begin{cases} 0 & T < T_{melting} - 0.5T_{window} \\ \frac{T-T_{melting}}{T_{window}} + 0.5 & T_{melting} - 0.5T_{window} < T < T_{melting} + 0.5T_{window} \\ 1 & T > T_{melting} + 0.5T_{window} \end{cases}; \tag{3}$$

controls the velocity components in the momentum domain. The symbols $T_{melting}$ and T_{window} are the melting and window temperatures.

$$\begin{aligned}\left[s(T)\left(\rho C_p\right)_{LNePCM} + (1-s(T))\left(\rho C_p\right)_{SNePCM}\right]\frac{DT}{Dt} = \\ \nabla\cdot\left([s(T)k_{LNePCM} + (1-s(T))k_{SNePCM}]\nabla T\right) + (VF_{na}-1)\rho_{PPCM}L_{PPCM}\frac{\partial s(T)}{\partial t}\end{aligned} \tag{4}$$

where temperature (T) is the dependent variable. Subscripts *SNePCM* and *PPCM* refer to the properties of the solid NePCM, and the pure PCM (without nanoparticles). Thermal conductivity coefficient (k), latent heat of phase transition (L), and heat capacity (C_p) are the thermophysical properties. VF_{na} represents the volume fraction of nanoparticles.

For the solid fin domain, the energy balance can be defined as the following:

$$\left(\rho C_p\right)_s\frac{\partial T}{\partial t} = \nabla\cdot(k_s\nabla T), \tag{5}$$

where the subscript s denotes the solid fin.

Assuming the fluid flow passing the tube is laminar and incompressible, the governing equations are:

$$\frac{D\vec{V}}{Dt} = 0, \tag{6}$$

$$\rho_{HTF}\frac{D\vec{V}}{Dt} = -\nabla p + \eta_{HTF}\nabla^2\vec{V}, \tag{7}$$

$$\left(\rho C_p\right)_{HTF}\frac{DT}{Dt} = \nabla\cdot\left(k_{HTF}\nabla T\right). \tag{8}$$

The subscript *HTF* points to heat transfer fluid (water) in the tube. The thermophysical characteristics of the nano-enhance phase change material are reached based on the relations listed below:

Density:

$$\rho_{NePCM} = (1 - VF_{na})\rho_{PPCM} + VF_{na}\rho_{na}; \tag{9}$$

$$\rho_{PPCM} = s(T)(\rho_{LPPCM} - \rho_{SPPCM}) + \rho_{SPPCM}. \tag{10}$$

PPCM denotes the properties of the pure phase change material.

Dynamic viscosity:

$$\eta_{LNePCM} = \frac{\eta_{LPPCM}}{(1 - VF_{na})^{2.5}}. \tag{11}$$

Coefficient of thermal expansion

$$\beta_{LNePCM} = \frac{\rho_{LPPCM}\beta_{LPPCM} - VF_{na}(\rho_{LPPCM}\beta_{LPPCM} - \rho_{na}\beta_{na})}{\rho_{LNePCM}}. \tag{12}$$

Thermal conductivity:

$$\frac{k_{L/SNePCM}}{k_{L/SPPCM}} = \frac{(k_{na} + 2k_{L/SPPCM}) - 2VF_{na}(k_{L/SPPCM} - k_{na})}{(k_{na} + 2k_{L/SPPCM}) + VF_{na}(k_{L/SPPCM} - k_{na})}. \tag{13}$$

Effective heat capacity:

$$C_{p,LNePCM} = \frac{\rho_{PPCM}C_{p,PPCM} - VF_{na}\left(\rho_{PPCM}C_{p,PPCM} - \rho_{na}C_{p,na}\right)}{\rho_{LNePCM}}. \tag{14}$$

$$C_{p,PPCM} = \frac{s(T)\left[\rho_{LPPCM}C_{p,LPPCM} - \rho_{SPPCM}C_{p,SPPCM}\right] + \rho_{SPPCM}C_{p,SPPCM}}{\rho_{PPCM}}. \tag{15}$$

The relevant initial and boundary conditions for the above equations are as follows.

At the interface of the tube and NePCM domain:

$$\left(k\frac{\partial T}{\partial r}\right)_{NePCM} = \left(k\frac{\partial T}{\partial r}\right)_{HTF},\ T_{HTF} = T_{NePCM}. \tag{16}$$

At the entrance of the tube:

$$T_{HTF} = 313K,\ (v_r)_{HTF} = 0,\ (v_z)_{HTF} = 0.01\ \mathrm{m/s}. \tag{17}$$

At the outlet tube:

$$(v_r)_{HTF} = 0,\ \left(\frac{\partial T}{\partial z}\right)_{HTF} = \left(\frac{\partial v_z}{\partial z}\right)_{HTF} = 0. \tag{18}$$

Also, the initial temperature of HTF, NePCM and fins is $T_{in} = 293$ K where the subscripts r and z are the coordinates in vertical (axial) and horizontal (radial) directions, respectively. At the vertical outer wall of the NePCM domain:

$$(v_r)_{NePCM} = (v_z)_{NePCM} = 0, \left(\frac{\partial T}{\partial r}\right)_{NePCM} = 0. \quad (19)$$

At the horizontal walls of the NePCM domain:

$$(v_r)_{NePCM} = (v_z)_{NePCM} = 0, \left(\frac{\partial T}{\partial z}\right)_{NePCM} = 0. \quad (20)$$

The pertinent initial condition of the NePCM zone:

$$(v_r)_{NePCM} = (v_z)_{NePCM} = 0, \; T_{in,NePCM} = 293 \text{ K}. \quad (21)$$

In the LHTES unit, the total stored energy is defined as the following:

$$ES(t) = \int_A \left[\rho_{LNePCM} C_{p,LNePCM}(T - T_{in}) + (1 - VF_{na})\rho_{PPCM} L_{PPCM}\right] dA. \quad (22)$$

The liquid fraction of NePCM during melting flow is expressed as:

$$MVF = \frac{A_{LNePCM}}{A_{LNePCM} + A_{SNePCM}}. \quad (23)$$

A_{LNePCM} is the area that NePCM is in liquid phase, and A_{SNePCM} is the non-melted NePCM area. To evaluate the uniformity of the temperature distribution, σ (t) can be defined as follows:

$$\sigma^2(t) = \int_A \left(T - T_{average}\right)^2 dA / \int_A dA. \quad (24)$$

$T_{average}$ indicates the average temperature of the PCM domain.

3. Numerical Approach and Grid Dependency

3.1. Solution Method

To find the fields of *MVF*, temperature, and velocity, we employed the numerical analysis by user defined finite element codes based on the Petrov–Galerkin approach. The governing equations were transformed into a weak form, and linear shape function (for heat equation) and quadratic Lagrange (for momentum equation) were applied. Then, the equations were integrated over mesh elements to obtain the residual equations. The residual equations were solved in the fully coupled form using the PARallel DIrect SOlver (PARDISO) [37,38] with a relative tolerance of 1×10^{-4}. A Newtonian damping factor of 0.9 was applied to enhance the convergence of the solver. The selection of the time-step is crucial in phase change problems with natural convection effects. Here, a backward differentiation formula (BDF) was used to control the computations' accuracy and convergence automatically. The details of the utilized finite element method and solution method can be found in [39,40].

To reach the high accuracy results, the mesh density was optimized through sensitivity analysis of the numerical results to the element numbers. Here a size parameter, NE, was introduced to control the size of mesh at various regions. The NE parameter was changed in the range of 0.75–1.75. A larger NE shows more elements and thus a fanner mesh. The details of the mesh elements in each region have been reported in Table 3. The mesh type in all domains is quad, and the mesh in the fins is structured, leading to rectangular mesh in the solid-fins domain. The reset of domains was filled with un-structured quad elements. The results of optimization can be found in Figure 3. As seen, the mesh with NE = 1.25 can be selected as the optimized grid.

Table 3. Details of mesh study and element sizes.

Case	NE	Element Number in Different Domains		
		HTF	Fins	PCM
1	0.75	1832	555	12,485
2	1.00	3080	1260	21,078
3	1.25	5432	1540	27,730
4	1.50	7472	2214	38,935
5	1.75	10,222	3480	51,090

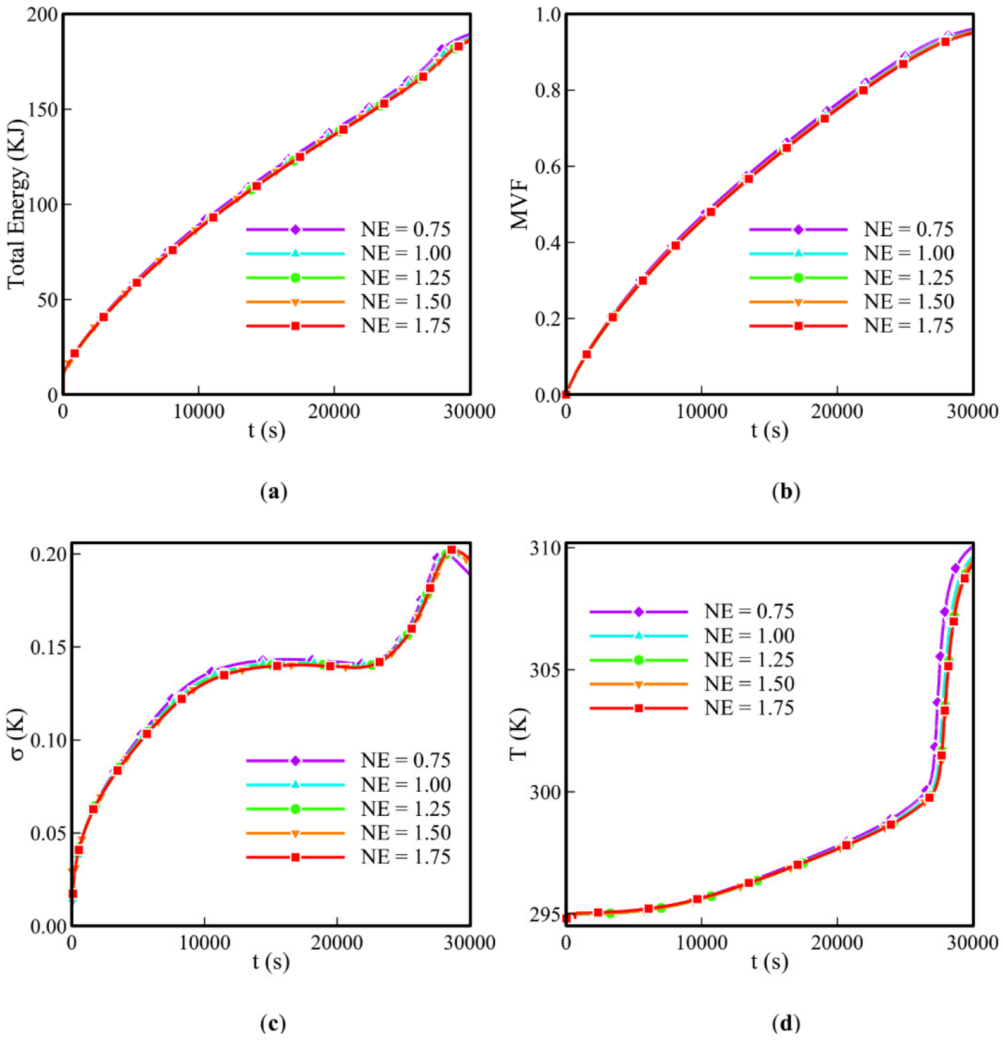

Figure 3. The effect of grid size for descending conical for a design with VF_{na} = 0.015, AR_f = 1.0, AR_c = 0.8, and GO nanoparticle. (**a**) Total energy stored; (**b**) melt volume fraction (MVF); (**c**) temperature uniformity; (**d**) temperature at P_4.

3.2. Validation of the Model with Literature Data

The implemented numerical model can be verified by employing a numerical analysis performed by Costa [41] and an experimental work conducted by Kumar et al. [42]. Costa [41] studied the influence of the thermal conductivity of the separators on the free convection in a partially divided cavity. Figure 4 shows the temperature distribution of the current model and that simulated by Costa [41]. The working fluid filling the cavity is air with a Prandtl number of 0.71. The left and right walls were subject to cold and hot isothermal temperatures. The domain temperatures were scaled for the temperature difference between the hot and cold walls. Thus, the isotherms are in the range of 0–1.

The natural convection Ryleigh number was 10^6. The partition walls were ten times more thermally conductive than the fluid inside the enclosure (air), and the size of the partition was 0.6 size of the enclosure, and the distance between the partition and side wall was 0.3 enclosure size.

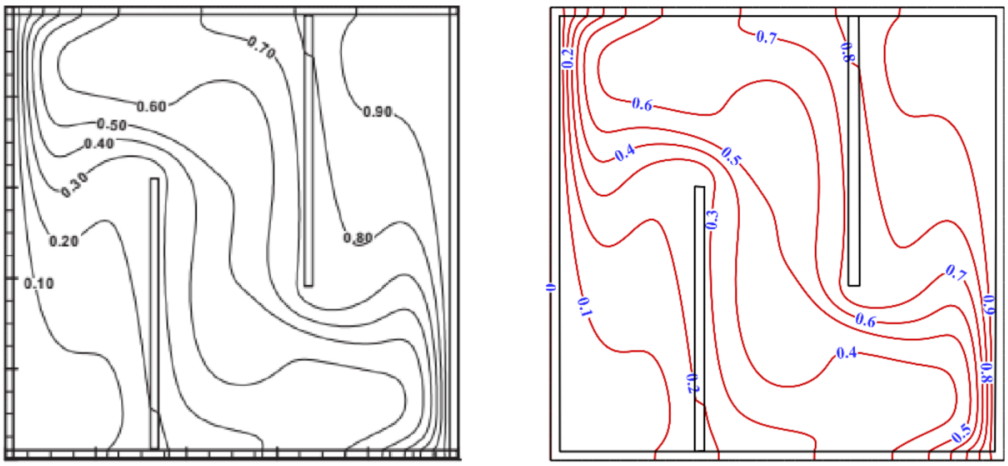

Work conducted by Costa [41] Present wrok

Figure 4. Temperature distributions of the work conducted by Costa [41] and the current isotherms.

In another validation, the liquid fraction field observed by Kumar et al. [42] which was also simulated by the current model are compared in Figure 5. The authors investigated the melting of lead in an enclosure with a height of 50 mm and an aspect ratio of 0.75 (height/width). The enclosure walls were well insulated except the right wall, which was subject to a constant heat flux (16.3 kW/m^2). The thermal neutron radiography method was used to map the melting interface. As seen, the melting starts from the right wall and advances toward the left. Moreover, due to the natural convection effects, the melting at the top is faster than at the bottom.

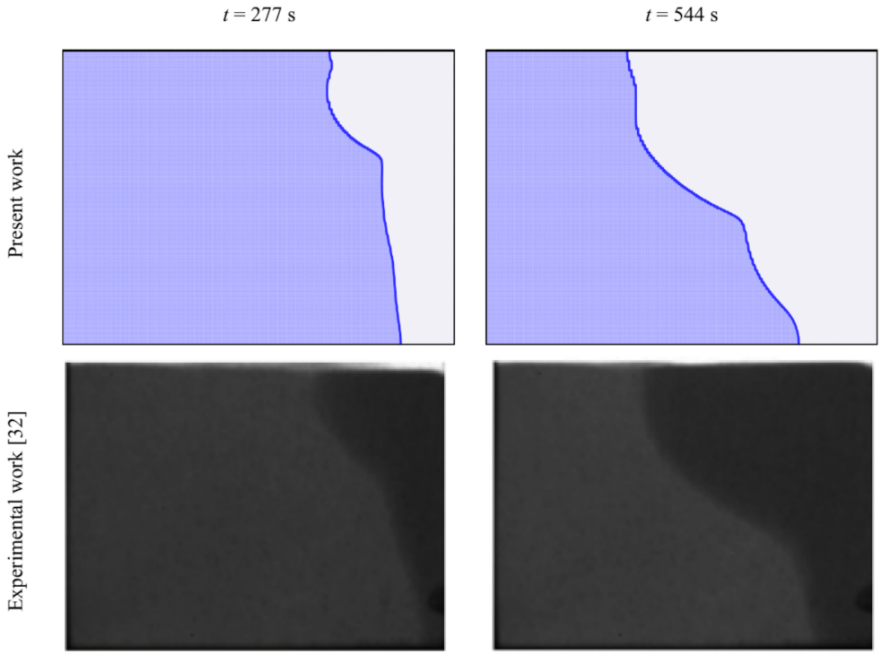

Figure 5. Melting fields of the present work and study conducted by [42].

In this comparison, the right side-wall of the cavity occupied by lead was exposed to a constant heat flux. The comparative analyses presented in Figures 4 and 5 confirm the reliability of the utilized code.

4. Results and Discussion

The present study aims to maximize the melting rate at seven hours of charging time. Here, the Taguchi optimization method is utilized to optimize four design parameters for the descending and ascending conical designs. The design parameters are the volume fraction of nanoparticles VF_{na} ($0 \leq VF_{na} \leq 0.045$), the ratio of the radius of the lower fin to the radius of the base fin ($0.1 \leq AR_f \leq 1.0$ for ascending conical and $1.0 \leq AR_f \leq 1.6$ for descending conical design), the ratio of the lower radius of conic to the radius of the regular cylinder ($0.4 \leq AR_c \leq 1.0$, $1.0 \leq AR_c \leq 1.5$), and type of nanoparticles. The type of nanoparticles could be Al_2O_3, GO (graphene oxide), Ag, and Cu. The amount of molten PCM is selected as the target design. Thus, "the higher, the better" design strategy was set for the Taguchi method. Each of the design parameters is divided into four levels. The details of the design parameters and their levels are summarized in Tables 4 and 5. These tables show the design for ascending and descending conical shells, respectively.

Table 4. The range and levels of design parameters for ascending conical shell.

Factors	Description	Level 1	Level 2	Level 3	Level 4
A	VF_{Na} (volume fraction)	0	0.015	0.03	0.045
B	AR_f (ratio of the radius of lower fin to the radius of the base fin)	0.1	0.4	0.7	1.0
C	AR_c (the ratio of the lower radius of conic to the radius of the regular cylinder)	0.4	0.6	0.8	1
D	*Nano* (type of nanoparticle)	Al_2O_3	GO	Ag	Cu

Table 5. The range and levels of design parameters for descending conical shell.

Factors	Description	Level 1	Level 2	Level 3	Level 4
A	VF_{Na} (volume fraction)	0	0.015	0.03	0.045
B	AR_f (ratio of the radius of lower fin to the radius of the base fin)	1	1.2	1.4	1.6
C	AR_c (the ratio of the lower radius of conic to the radius of the regular cylinder)	1	1.17	1.33	1.5
D	Nano (type of nanoparticle)	Al_2O_3	GO	Ag	Cu

The combination of four design parameters and four levels leads to 4^4 possible design combinations for each shell geometry. Simulating all possible combinations requires a tremendous computational budget. Thus, Taguchi uses an orthogonal table to reduce the required simulations. Here, the standard orthogonal L16 table has been selected for each design geometry. Tables 6 and 7 show the L16 design cases for each of the ascending and descending conical shells, respectively.

The melting phase change simulations were executed for each of the design cases of L16 Tables 6 and 7. Then, the values of MVF and Total stored energy (*ES*) after seven-hours of charging (melting) were reported in the Tables. The Taguchi method was used to compute the values of the S/N ratio based on the values of MVF. Since the target is "the higher, the better," a larger value of S/N ratio shows a better-designed case. The Taguchi method uses these S/N ratios to find the best level of each design parameter and reach a final optimum design.

Table 6. The L16 Taguchi table for ascending conical shell geometry.

Case	A VF_{Na}	B AR_f	C AR_c	D Nano	Value at 7 h *MVF*	*ES* (kJ)	S/N Ratio
1	0.000	0.1	0.4	1	0.77	149.4	−2.27019
2	0.000	0.4	0.6	2	0.83	160.3	−1.61844
3	0.000	0.7	0.8	3	0.88	170.0	−1.11035
4	0.000	1.0	1.0	4	0.90	165.0	−0.91515
5	0.015	0.1	0.6	3	0.85	161.6	−1.41162
6	0.015	0.4	0.4	4	0.77	149.6	−2.27019
7	0.015	0.7	1.0	1	0.92	167.9	−0.72424
8	0.015	1.0	0.8	2	0.87	168.3	−1.20961
9	0.030	0.1	0.8	4	0.91	161.9	−0.81917
10	0.030	0.4	1.0	3	0.91	173.1	−0.81917
11	0.030	0.7	0.4	2	0.77	146.2	−2.27019
12	0.030	1.0	0.6	1	0.80	154.6	−1.93820
13	0.045	0.1	1.0	2	0.88	166.3	−1.11035
14	0.045	0.4	0.8	1	0.95	180.6	−0.44553
15	0.045	0.7	0.6	4	0.85	162.8	−1.41162
16	0.045	1.0	0.4	3	0.75	142.1	−2.49877

Table 7. The L16 Taguchi table for descending conical shell geometry.

Case	A VF_{Na}	B AR_f	C AR_c	D Nano	Value at 7 h MVF	ES (kJ)	S/N Ratio
1	0.000	1.0	1.00	1	0.90	165.1	−0.91515
2	0.000	1.2	1.17	2	0.90	164.3	−0.91515
3	0.000	1.4	1.33	3	0.86	163.7	−1.31003
4	0.000	1.6	1.50	4	0.79	151.2	−2.04746
5	0.015	1.0	1.17	3	0.90	173.0	−0.91515
6	0.015	1.2	1.00	4	0.92	173.2	−0.72424
7	0.015	1.4	1.50	1	0.78	150.2	−2.15811
8	0.015	1.6	1.33	2	0.88	160.7	−1.11035
9	0.030	1.0	1.33	4	0.84	159.8	−1.51441
10	0.030	1.2	1.50	3	0.78	147.8	−2.15811
11	0.030	1.4	1.00	2	0.90	172.6	−0.91515
12	0.030	1.6	1.17	1	0.91	164.7	−0.81917
13	0.045	1.0	1.50	2	0.76	142.7	−2.38373
14	0.045	1.2	1.33	1	0.88	165.4	−1.11035
15	0.045	1.4	1.17	4	0.96	176.8	−0.35458
16	0.045	1.6	1.00	3	0.87	166.1	−1.20961

Figures 6 and 7 show the values of the S/N ratio for each level of each design parameter for two geometrical designs of ascending and descending conical shells. From Figure 6, it can be found that the maximum S/N values correspond to VF_{na} = 0.045, AR_f = 0.4, AR_c = 1.0, and Al_2O_3 nanoparticles for ascending design. The optimum design levels for descending design could be found in Figure 7, as follows: VF_{na} = 0.015, AR_f = 1.4, AR_c = 1.17, and Cu nanoparticles. The optimum design parameters and the estimated values of MVF by the Taguchi method are summarized in Table 8. Numerical simulations were also executed for these optimum cases, and the computed MVF is reported in Table 8. The simulated cases show an MVF = 0.92 after seven hours of thermal charging for both ascending and descending designs. These values are greater than equal to the simulated case of L16 tables. Thus, they have been selected as optimum designs.

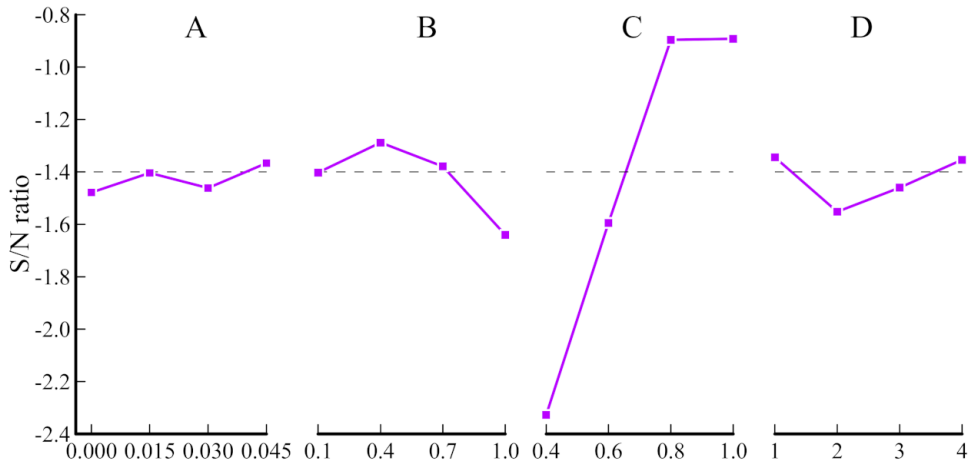

Figure 6. The S/N ratios for all the levels of the design parameters for ascending conical shell.

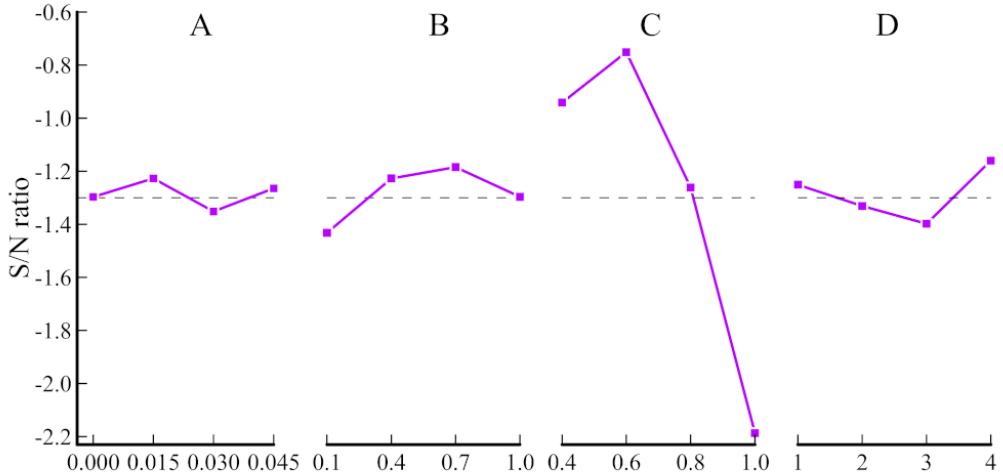

Figure 7. The S/N ratios for all the levels of the design parameters for descending conical shell.

Table 8. The optimum values of the design parameters and MVF.

Type	Optimum Factors				Optimum MVF at 7 h	
	VF_{na}	AR_f	AR_c	Nano	Taguchi Prediction	Numerical Simulations
Ascending	0.045	0.4	1.0	Al_2O_3	0.93	0.92
Descending	0.015	1.4	1.17	Cu	0.95	0.92

It should be noted that the range of the variation of S/N in Figures 6 and 7 shows the impact of a design parameter on the MVF. As seen, the most significant parameter is AR_c for both cases. This parameter indicates the ratio of the lower radius of conic to the radius of the regular cylinder. The next important design parameter is AR_f, which represents the ratio of the radius of the lower fin to the radius of the base fin. The other less important design variables are the type of nanoparticles and the volume fraction of nanoparticles. Thus, special attention should be made to selecting shell ratio (AR_c) and fin ratio (AR_f). Then, the LHTES unit's charging rate can be fine-tuned by selecting the type and volume fraction of nanoparticles.

For ascending conical shell geometry, the minimum *MVF* corresponds to case 16 Table 6 with *MVF* = 0.75. Thus, the optimum case with *MVF* = 0.92 increases the melting rate by 18.5% compared to this case. The lowest *MVF* = 0.76 corresponds to case 13 of

Table 7 for a descending design. Since the optimum case is *MVF* = 0.92, a 17.3% increase of *MVF* can be achieved by an optimum design.

Figure 8 shows the melting maps of NEPCM for the optimum case of ascending conical shell. The results are reported at seven different time steps during the melting process. Figure 9 depicts the isotherm maps for the same snapshots of Figure 6. As seen, the melting commences around the tube wall and fins. Then, it advances in the enclosure toward the adiabatic shell. At t = 3750 s, small circulation cells between fins can be seen in molten regions. The circulation extends to a large portion of the enclosure by the advancement of melting, and a single central circulation occurs at t = 15,000 s and beyond. The solid zones quickly disappear at the top of the enclosure due to the circulation flows and long fins at the top. The only un-melted region at 26,250 s is at the bottom of the enclosure. This region slowly melts down as time passes. Figure 9 shows that the HTF in the tube is mostly at a uniform hot temperature. Only at the initial charging stages, a smooth low-temperature boundary layer next to the tube wall can be seen. At 7500 s and larger, the heat transfer rate at the PCM sides drops notability, and the temperature of HTF in the tube is uniformly hot. It is interesting that the temperature of the molten PCM reaches the HTF temperature at the top regions of the enclosure, where there is a small amount of solid PCM at the bottom.

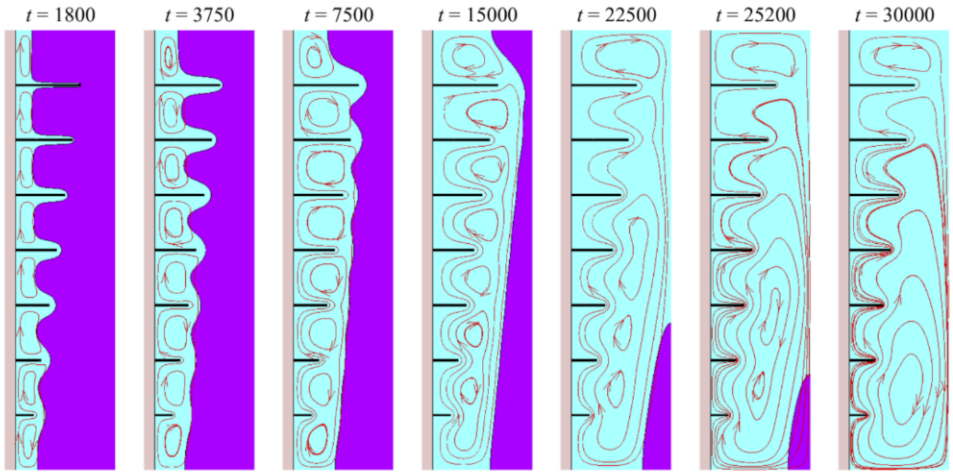

Figure 8. Melting maps and streamlines of ascending conical shell. The purple region is solid nano-enhanced phase change material (NePCM) and the blue region is molten NePCM at various t (s).

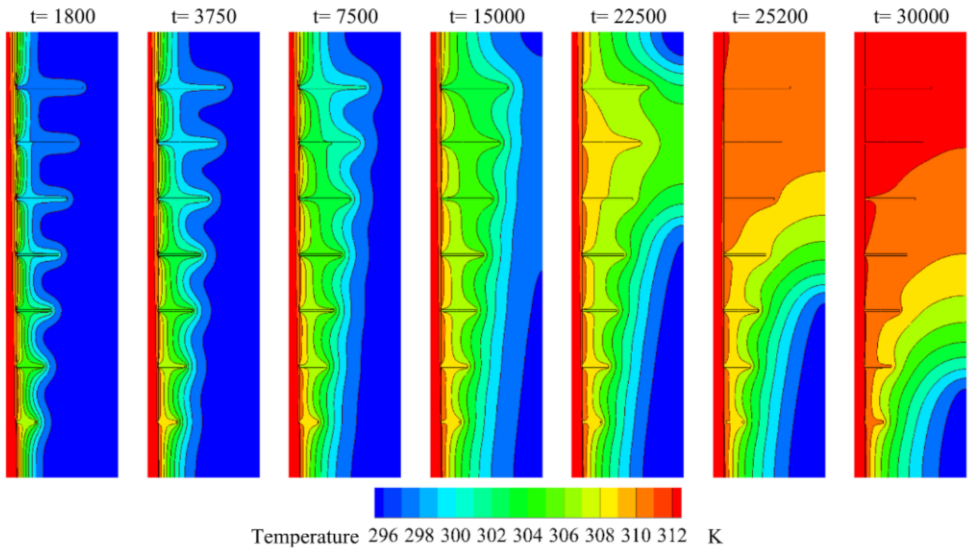

Figure 9. Isotherm maps of an ascending conical shell. From left to right hand at various *t* (s).

Figures 10 and 11 show melting fraction maps and the temperature in the optimum design of an ascending conical shell. As seen in this design, the fins are long at the bottom and short at the top. The shell is also wide at the bottom and narrow at the top. In the descending case, the same as the ascending one, the melting commences from the tube wall and around the fins and advances into the enclosure toward the shell. However, in this design, there is a narrow space between the tube and con-shell at the top. This narrow space breaks the main circulation flow into two distinct circulation flows. The PCM melts uniformly next to the cone shell. Thus, a smaller piece of solid PCM can be seen at the bottom at t = 22,500 s compared to the ascending design. Moreover, the hot molten PCM is in the middle of the enclosure and advances toward the corners.

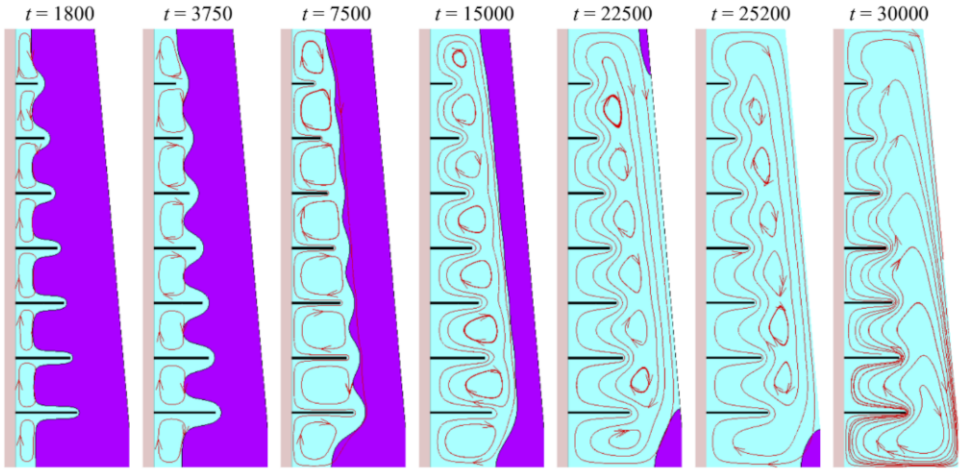

Figure 10. Melting maps and streamlines of descending conical shell. The purple region is solid NePCM and the blue region is molten NePCM. From left to right hand at various *t* (s).

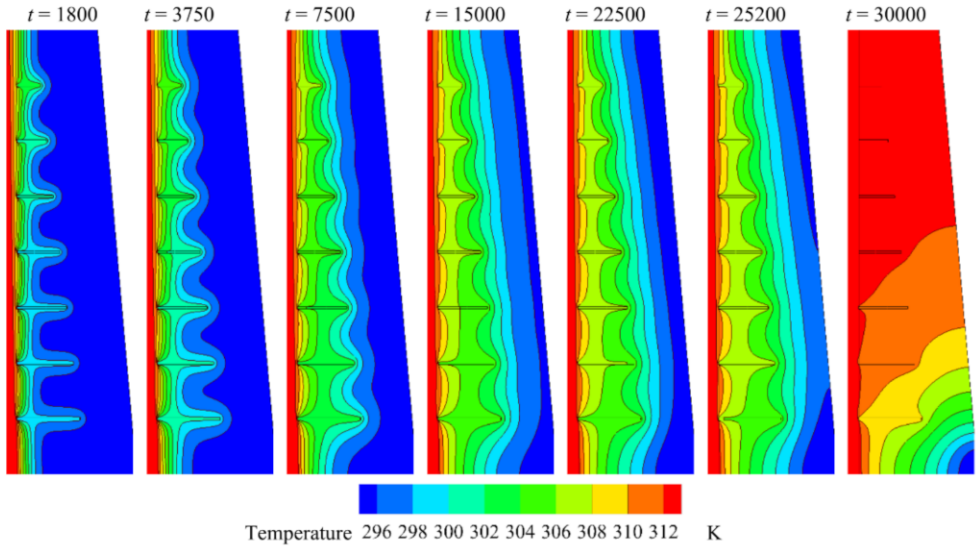

Figure 11. Isotherm maps of descending conical shell. From left to right hand at various *t* (s).

Figure 12 shows the temperature variation of eight monitor points in each of the ascending and descending designs. The monitor points are depicted in Table 9. The points start from the bottom and move upward. As seen, all of the temperature points are initially at a supper cold temperature of 293 K. Then, the temperature sharply increases to about 295 K. This sharp rise of temperature corresponds to the solid region's conduction heat transfer. Then the phase change occurs, and the rise of the temperature limits to the phase change temperature bond. In this situation, the heat transfer does not increase the

temperature notably, and the heat stores in the PCM in the form of latent heat. Once the PCM at the monitor point melts down, the temperature rises again. The rise of temperature at the end of the melting process is due to the increase of temperature in the molten PCM. The monitor points at the top of the enclosure tend to quickly reach about 313 K, which is the temperature of HTF. The monitor points show a short phase change history for the case of ascending design. The melting maps also showed that the bottom of the enclosure remains at solid state during most of the charging time. Figure 12b shows the monitor points have almost similar behavior since the melting front advances in the enclosure uniformly toward the enclosure shell.

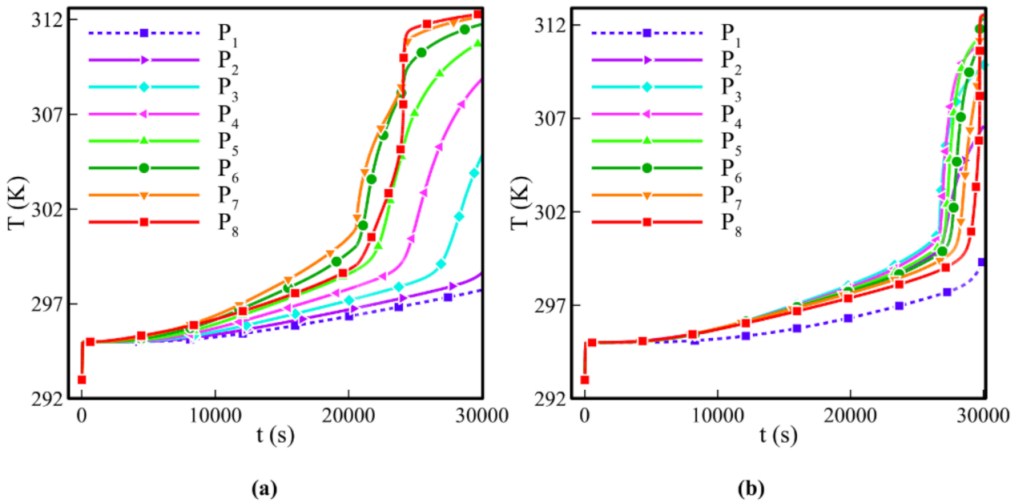

Figure 12. The temperature variation of the monitor points for two cases of: (**a**) optimum ascending design; (**b**) optimum descending design.

Table 9. The coordinate of temperature monitor points in optimum ascending and descending designs.

Point	Ascending Design		Descending Designs	
	r (mm)	z (mm)	r (mm)	z (mm)
1	40	8	48	8
2	40	33	46	33
3	40	58	43	58
4	40	83	41	83
5	40	108	39	108
6	40	133	37	133
7	40	158	35	158
8	40	183	32	183

Figure 13a–c show the melted portion (MVF), total stored energy (ES), and temperature non-uniformity (σ) during the melting process, respectively. The results are plotted for two ascending and descending designs. As seen, the descending designs lead to a higher MVF during the charging process.

Only at the final stages of melting, the ascending design is better than the descending design. Thus, for applications in which the full charging is not very important and about 85% of charging is adequate, then the descending design can be selected. However, when the full melting is the main target of design, the ascending design should be selected.

Figure 13b shows that the total stored energy for the case of ascending design is also higher around the final stage of charging (just before full charging). The temperature non-uniformity for the ascending design is higher than the case of the descending design at the end of the charging process. This is because the top of the ascending design at the end

of the charging process is at a hot temperature and subject to natural convection while its bottom is not melted yet. Thus, the LHTES unit is subject to high-temperature differences.

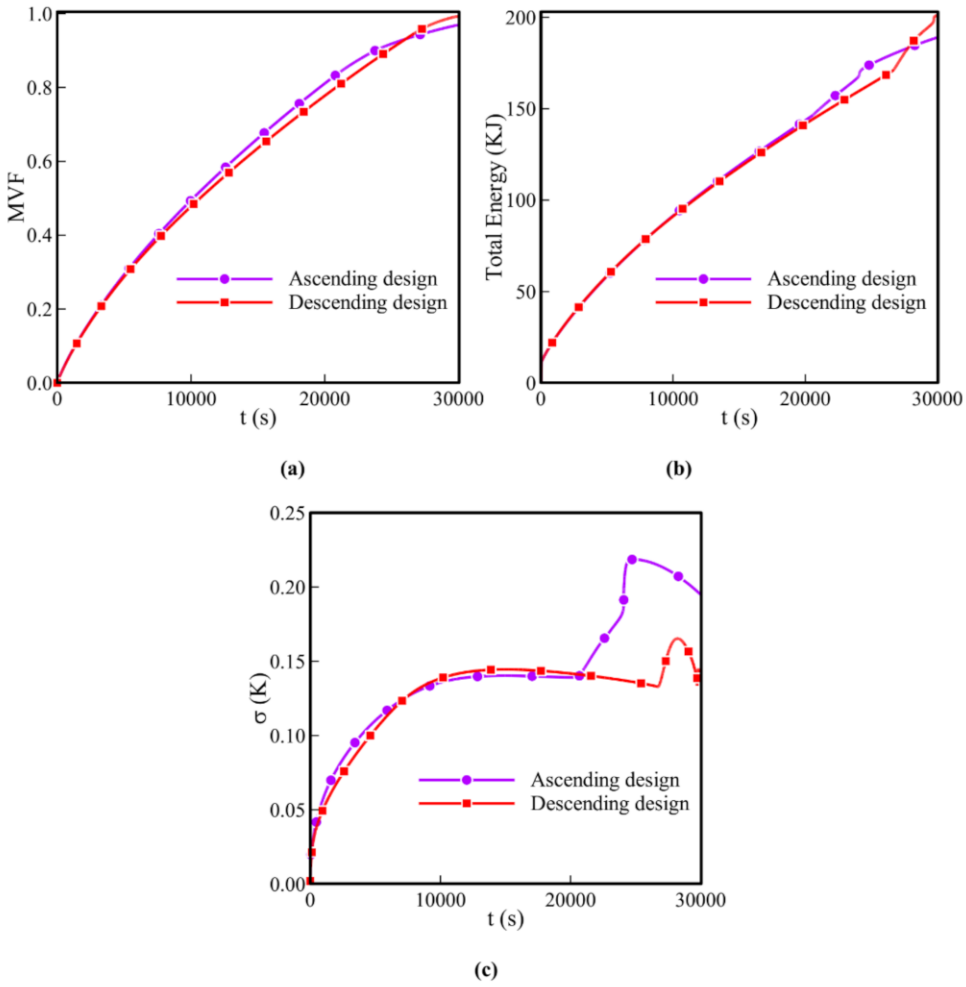

Figure 13. The variation of characteristic parameters for the ascending and descending designs. (**a**) MVF; (**b**) total stores energy; (**c**) temperature uniformity.

The results of Figure 6 show that the presence of nanoparticles could induce a minor impact on MVF, and the increase of the concentration of nanoparticles does not improve MVF monastically. These findings are in agreement with the results of the experimental investigation of Li et al. [30]. The experimental results show that the presence of nanoparticles increases both thermal conductivity and dynamic viscosity. Thus, using NePCMs could benefit conduction-dominant regimes where the heat transfer is under the direct influence of thermal conductivity while the dynamic viscosity is not important. However, as the melting advances and natural convection flows occur the dynamic viscosity influences the intensity of liquid circulation. Thus, the growth of viscosity due to the presence of nanoparticles could slow down the natural convection effects. It should also be noted that the natural convection effects are under the influence of geometrical design (enclosure shape and fins), and therefore, the combination of these effects should be taken into account in the heat transfer design of LHTES systems.

Currently, various types of NePCMs are being synthesized by various researchers. Some of these works have been reviewed by Leong et al. [43] and Nižetić [44]. The analysis of synthesized NePCM samples shows that the presence of nanoparticles changes the host PCM's thermophysical properties. It should be noted that the heat transfer performance of LHTES systems is a nonlinear function of the thermophysical properties

and their geometrical design. Thus, numerical simulations/experimental studies are demanded to investigate the advantage/drawback of using NePCMs. The present study took into account the combination of geometrical factors and the presence of nanoparticles to analyze the heat transfer behavior of LHTES systems for various concentrations and types of nanoparticles.

5. Conclusions

The melting heat transfer and thermal energy storage in a conical-shell LHTES unit filled with nano-enhanced phase change materials were addressed. The melting heat transfer was enhanced by applying a non-uniform array of fins. Two possible shell-designs, ascending and descending designs, were investigated. Four types of nanoparticles were examined. For each design, the volume fraction and type of nanoparticles, the shell aspect ratio, and the fin aspect ratio were optimized using the Taguchi method for maximum melting rate. The major finding of the current research can be summarized as follows:

- The most important parameter influencing the melting rate is the aspect ratio of the shell (AR_c). The optimum AR_c for the ascending design was 1.0 (a cylindrical shell), and for the descending design, it was 1.17.
- The fins arrangement was the second most important design parameter, influencing the melting rate. The best fin aspect ratios were the cases with a smooth variation of fin sizes. Thus, the middle size values of AR_f = 0.4 and 1.4 for ascending and descending designs were led to optimum melting rate, respectively. The melting maps showed that the fins significantly contribute to heat transfer at the initial stages of melting, where the heat transfer is conduction dominant. However, at the final stages of melting, the natural convection circulations play an important role in melting heat transfer. The fins' arrangement is crucial since long fins could suppress the natural convection flows.
- The type of nanoparticles was the third most important design parameter, influencing the melting rate. The optimum type of nanoparticles depends on the designed geometry. Alumina nanoparticles were the best for an ascending design, while copper nanoparticles were a better choice for a descending design. Indeed, the presence of nanoparticles influences the heat capacity and thermal conductivity of the NePCM. Thus, the type of these nano-additives should be selected carefully.
- The presence of nanoparticles could improve the melting rate. However, the best volume fraction of nanoparticles for a descending design was only 1.5% of nanoparticles, while the maximum possible volume fraction could be 4.5%. This shows that the increase in the volume fraction of the nanoparticles is not always advantageous. The nanoparticles increase the dynamic viscosity of molten NePCM, and thus, they can weaken the natural convection flows.

Author Contributions: Conceptualization, M.G., S.A.M.M. and M.M.; methodology, M.G., S.A.M.M., M.M., O.Y. and M.A.A.; software, S.A.M.M.; validation, S.A.M.M.; formal analysis, M.G. and S.A.M.M.; and M.A.A.; investigation, M.G., S.A.M.M., M.M., O.Y. and M.A.A.; resources, M.G., O.Y. and M.A.A.; writing—original draft preparation, M.G., S.A.M.M., M.M., O.Y. and M.A.A.; writing—review and editing, M.G., S.A.M.M., M.M., O.Y. and M.A.A.; visualization, S.A.M.M. and M.G; supervision, M.G. All authors have read and agreed to the published version of the manuscript.

Funding: This research received no external funding.

Institutional Review Board Statement: Not applicable.

Informed Consent Statement: Not applicable.

Data Availability Statement: Data is contained within the article.

Conflicts of Interest: The authors declare no conflict of interest.

Nomenclature

A	surface area of domain, m^2
a	slope of the outer surface of the shell, $(R_{uc} - R_{dc})/L$
A_m	mushy parameter, kg m^{-3} s^{-1}
AR_c	ratio of the lower radius of the conical shell to the radius of the uniform cylindrical shell, $AR_c = R_{dc}/R_o$
AR_f	ratio of the length of lowest fin to the length of identical fin, w_{df}/w_{uf}
C_p	specific heat capacity, J kg^{-1} K^{-1}
d	distance between two adjacent fins, m
ES	total stored energy, kg m^2 s^{-2}
g	gravitational acceleration, m s^{-2}
h_{sf}	distance between the lowest fin and the lower surface of the shell, mm
k	thermal conductivity, kg m^2 s^{-3} K^{-1}
L	melting latent, m^2 s^{-2}; heat storage height, m
MVF	melting volume fraction
$Nano$	type of nanoparticle
NE	parameter for mesh size control
p	pressure, kg m^{-1} s^{-2}
P_i	monitor points
r, z	coordinate system, m
R_{dc}	lower radius of the cylindrical shell, mm
R_i	heating tube radius, m
R_o	radius of the uniform cylindrical shell, m
R_{uc}	upper radius of the cylindrical shell, mm
s	local liquid fraction
S/N	signal to noise ratio
t	time s; fin's thickness, m
T	temperature, K
T_{in}	initial temperature, K
$T_{melting}$	melting temperature, K
$\vec{V}$	velocity vector, m
VF_{na}	concentration of nanoparticles
v_r, v_z	r, z velocities directions, m s^{-1}
w_{df}	length of the lowest fin, m
w_f	fin length, m
w_{uf}	length of the top fin, m
Greek	
μ	dynamic viscosity, kg s^{-1} m^{-1}
β	thermal expansion coefficient, K^{-1}
ρ	density, kg m^{-3}
σ	parameter of the temperature distribution, K
Subscripts	
average	average property
HTF	heat transfer fluid
LNePCM	nano-enhanced phase change material at liquid phase
NePCM	nano-enhanced phase change material
PPCM	pure phase change material
s	sold fins
SNePCM	nano-enhanced phase change material at solid phase

References

1. Mahdi, J.M.; Lohrasbi, S.; Nsofor, E.C. Hybrid heat transfer enhancement for latent-heat thermal energy storage systems: A review. *Int. J. Heat Mass Transf.* **2019**, *137*, 630–649. [CrossRef]
2. Maldonado, J.M.; De Gracia, A.; Cabeza, L.F. Systematic review on the use of heat pipes in latent heat thermal energy storage tanks. *J. Energy Storage* **2020**, *32*, 101733. [CrossRef]
3. Shabgard, H.; Bergman, T.L.; Sharifi, N.; Faghri, A. High temperature latent heat thermal energy storage using heat pipes. *Int. J. Heat Mass Transf.* **2010**, *53*, 2979–2988. [CrossRef]

4. Xiong, T.; Zheng, L.; Shah, K.W. Nano-enhanced phase change materials (NePCMs): A review of numerical simulations. *Appl. Therm. Eng.* **2020**, *178*, 115492. [CrossRef]
5. Hosseinizadeh, S.F.; Darzi, A.A.R.; Tan, F.L. Numerical investigations of unconstrained melting of nano-enhanced phase change material (NEPCM) inside a spherical container. *Int. J. Therm. Sci.* **2012**, *51*, 77–83. [CrossRef]
6. Elbahjaoui, R.; El Qarnia, H. Thermal analysis of nanoparticle-enhanced phase change material solidification in a rectangular latent heat storage unit including natural convection. *Energy Build.* **2017**, *153*, 1–17. [CrossRef]
7. Pahamli, Y.; Hosseini, M.J.; Ranjbar, A.A.; Bahrampoury, R. Effect of nanoparticle dispersion and inclination angle on melting of PCM in a shell and tube heat exchanger. *J. Taiwan Inst. Chem. Eng.* **2017**, *81*, 316–334. [CrossRef]
8. Parsazadeh, M.; Duan, X. Numerical study on the effects of fins and nanoparticles in a shell and tube phase change thermal energy storage unit. *Appl. Energy* **2018**, *216*, 142–156. [CrossRef]
9. Iachachene, F.; Haddad, Z.; Oztop, H.F.; Abu-Nada, E. Melting of phase change materials in a trapezoidal cavity: Orientation and nanoparticles effects. *J. Mol. Liq.* **2019**, *292*, 110592. [CrossRef]
10. Kant, K.; Shukla, A.; Sharma, A.; Henry Biwole, P. Heat transfer study of phase change materials with graphene nano particle for thermal energy storage. *Solar Energy* **2017**, *146*, 453–463. [CrossRef]
11. Lin, S.C.; Al-Kayiem, H.H. Evaluation of copper nanoparticles—Paraffin wax compositions for solar thermal energy storage. *Solar Energy* **2016**, *132*, 267–278. [CrossRef]
12. Mahdi, J.M.; Nsofor, E.C. Solidification of a PCM with nanoparticles in triplex-tube thermal energy storage system. *Appl. Therm. Eng.* **2016**, *108*, 596–604. [CrossRef]
13. Hajighafoori Boukani, N.; Dadvand, A.; Chamkha, A.J. Melting of a Nano-enhanced Phase Change Material (NePCM) in partially-filled horizontal elliptical capsules with different aspect ratios. *Int. J. Mech. Sci.* **2018**, *149*, 164–177. [CrossRef]
14. Gharebaghi, M.; Sezai, I. Enhancement of Heat Transfer in Latent Heat Storage Modules with Internal Fins. *Numer. Heat Transf. Part A Appl.* **2007**, *53*, 749–765. [CrossRef]
15. Rahimi, M.; Ranjbar, A.A.; Ganji, D.D.; Sedighi, K.; Hosseini, M.J.; Bahrampoury, R. Analysis of geometrical and operational parameters of PCM in a fin and tube heat exchanger. *Int. Commun. Heat Mass Transf.* **2014**, *53*, 109–115. [CrossRef]
16. Yang, X.; Lu, Z.; Bai, Q.; Zhang, Q.; Jin, L.; Yan, J. Thermal performance of a shell-and-tube latent heat thermal energy storage unit: Role of annular fins. *Appl. Energy* **2017**, *202*, 558–570. [CrossRef]
17. Khan, Z.; Khan, Z.A. An experimental investigation of discharge/solidification cycle of paraffin in novel shell and tube with longitudinal fins based latent heat storage system. *Energy Convers. Manag.* **2017**, *154*, 157–167. [CrossRef]
18. Mahdi, J.M.; Lohrasbi, S.; Ganji, D.D.; Nsofor, E.C. Accelerated melting of PCM in energy storage systems via novel configuration of fins in the triplex-tube heat exchanger. *Int. J. Heat Mass Transf.* **2018**, *124*, 663–676. [CrossRef]
19. Kazemi, M.; Hosseini, M.; Ranjbar, A.; Bahrampoury, R. Improvement of longitudinal fins configuration in latent heat storage systems. *Renew. Energy* **2018**, *116*, 447–457. [CrossRef]
20. Deng, S.; Nie, C.; Wei, G.; Ye, W.-B. Improving the melting performance of a horizontal shell-tube latent-heat thermal energy storage unit using local enhanced finned tube. *Energy Build.* **2019**, *183*, 161–173. [CrossRef]
21. Rathod, M.K.; Banerjee, J. Thermal performance enhancement of shell and tube Latent Heat Storage Unit using longitudinal fins. *Appl. Therm. Eng.* **2015**, *75*, 1084–1092. [CrossRef]
22. Mahdi, J.M.; Nsofor, E.C. Solidification enhancement of PCM in a triplex-tube thermal energy storage system with nanoparticles and fins. *Appl. Energy* **2018**, *211*, 975–986. [CrossRef]
23. Mahdi, J.M.; Lohrasbi, S.; Ganji, D.D.; Nsofor, E.C. Simultaneous energy storage and recovery in the triplex-tube heat exchanger with PCM, copper fins and Al_2O_3 nanoparticles. *Energy Convers. Manag.* **2019**, *180*, 949–961. [CrossRef]
24. Tiari, S.; Qiu, S.; Mahdavi, M. Numerical study of finned heat pipe-assisted thermal energy storage system with high temperature phase change material. *Energy Convers. Manag.* **2015**, *89*, 833–842. [CrossRef]
25. Nakhchi, M.E.; Hatami, M.; Rahmati, M. A numerical study on the effects of nanoparticles and stair fins on performance improvement of phase change thermal energy storages. *Energy* **2021**, *215*, 119112. [CrossRef]
26. u Mekrisuh, K.; Giri, S.; Udayraj; Singh, D.; Rakshit, D. Optimal design of the phase change material based thermal energy storage systems: Efficacy of fins and/or nanoparticles for performance enhancement. *J. Energy Storage* **2021**, *33*, 102126. [CrossRef]
27. Mahdi, J.M.; Mohammed, H.I.; Hashim, E.T.; Talebizadehsardari, P.; Nsofor, E.C. Solidification enhancement with multiple PCMs, cascaded metal foam and nanoparticles in the shell-and-tube energy storage system. *Appl. Energy* **2020**, *257*, 113993. [CrossRef]
28. Liang, L.; Diao, Y.H.; Zhao, Y.H.; Wang, Z.Y.; Bai, F.W. Numerical and experimental investigations of latent thermal energy storage device based on a flat micro-heat pipe array–metal foam composite structure. *Renew. Energy* **2020**, *161*, 1195–1208. [CrossRef]
29. Ren, Q.; Xu, H.; Luo, Z. PCM charging process accelerated with combination of optimized triangle fins and nanoparticles. *Int. J. Therm. Sci.* **2019**, *140*, 466–479. [CrossRef]
30. Li, Z.-R.; Hu, N.; Liu, J.; Zhang, R.-H.; Fan, L.-W. Revisiting melting heat transfer of nano-enhanced phase change materials (NePCM) in differentially-heated rectangular cavities using thermochromic liquid crystal (TLC) thermography. *Int. J. Heat Mass Transf.* **2020**, *159*, 120119. [CrossRef]
31. Rabienataj Darzi, A.A.; Jourabian, M.; Farhadi, M. Melting and solidification of PCM enhanced by radial conductive fins and nanoparticles in cylindrical annulus. *Energy Convers. Manag.* **2016**, *118*, 253–263. [CrossRef]
32. Al-Jethelah, M.; Ebadi, S.; Venkateshwar, K.; Tasnim, S.H.; Mahmud, S.; Dutta, A. Charging nanoparticle enhanced bio-based PCM in open cell metallic foams: An experimental investigation. *Appl. Therm. Eng.* **2019**, *148*, 1029–1042. [CrossRef]

33. Choi, S.-K.; Kim, S.-O.; Lee, T.-H.; Dohee-Hahn. Computation of the natural convection of nanofluid in a square cavity with homogeneous and nonhomogeneous models. *Numer. Heat Transf. Part A Appl.* **2014**, *65*, 287–301. [CrossRef]
34. Bondareva, N.S.; Buonomo, B.; Manca, O.; Sheremet, M.A. Heat transfer inside cooling system based on phase change material with alumina nanoparticles. *Appl. Therm. Eng.* **2018**, *144*, 972–981. [CrossRef]
35. Turkyilmazoglu, M.; Pop, I. Heat and mass transfer of unsteady natural convection flow of some nanofluids past a vertical infinite flat plate with radiation effect. *Int. J. Heat Mass Transf.* **2013**, *59*, 167–171. [CrossRef]
36. Öğüt, E.B. Natural convection of water-based nanofluids in an inclined enclosure with a heat source. *Int. J. Therm. Sci.* **2009**, *48*, 2063–2073. [CrossRef]
37. Schenk, O.; Gärtner, K. Solving unsymmetric sparse systems of linear equations with PARDISO. *Future Gener. Comput. Syst.* **2004**, *20*, 475–487. [CrossRef]
38. Bollhöfer, M.; Eftekhari, A.; Scheidegger, S.; Schenk, O. Large-scale sparse inverse covariance matrix estimation. *SIAM J. Sci. Comput.* **2019**, *41*, A380–A401. [CrossRef]
39. Girault, V.; Raviart, P.-A. *Finite Element Methods for Navier-Stokes Equations: Theory and Algorithms*; Springer Science & Business Media: Berlin, Germany, 2012; Volume 5.
40. Thomasset, F. *Implementation of Finite Element Methods for Navier-Stokes Equations*; Springer Science & Business Media: Berlin, Germany, 2012.
41. Costa, V. Natural convection in partially divided square enclosures: Effects of thermal boundary conditions and thermal conductivity of the partitions. *Int. J. Heat Mass Transf.* **2012**, *55*, 7812–7822. [CrossRef]
42. Kumar, L.; Manjunath, B.; Patel, R.; Markandeya, S.; Agrawal, R.; Agrawal, A.; Kashyap, Y.; Sarkar, P.; Sinha, A.; Iyer, K. Experimental investigations on melting of lead in a cuboid with constant heat flux boundary condition using thermal neutron radiography. *Int. J. Therm. Sci.* **2012**, *61*, 15–27. [CrossRef]
43. Leong, K.Y.; Rahman, M.R.A.; Gurunathan, B.A. Nano-enhanced phase change materials: A review of thermo-physical properties, applications and challenges. *J. Energy Storage* **2019**, *21*, 18–31. [CrossRef]
44. Nižetić, S.; Jurčević, M.; Arıcı, M.; Arasu, A.V.; Xie, G. Nano-enhanced phase change materials and fluids in energy applications: A review. *Renew. Sustain. Energy Rev.* **2020**, *129*, 109931. [CrossRef]